Original Article

Characterization and Antimicrobial Activity of Biosynthesized Iron (III) Oxide Nanoparticles Stabilized by *Luffa cylindrica* Extract

Azaki Gideon Philip[1*], Adamu Makanta Salihu[1, 2], Fadipe Labake Ajoke[1], Shaba Elijah Yanda[1, 3], Agbai Uche Timothy[4], James Daniel[5], Suleiman Rahmat[1, 6]

1. Department of Chemistry, School of Physical Sciences, Federal University of Technology, Minna, Nigeria.
2. Department of Chemistry and Biochemistry, Sharda School of Basic Sciences and Research (SSBSR), Sharda University, Greater Noida, India.
3. Nanotechnology Research Group, Africa Centre of Excellence for Mycotoxin and Food Safety, Federal University of Technology, Minna, Nigeria.
4. Department of Chemistry and Biochemistry, College of Engineering and Physical Sciences, University of New Hampshire, Durham, United States.
5. Wuhan Institute of Virology, University of Chinese Academy of Sciences, Beijing, China.
6. Department of Chemistry, Niger State College of Education, Minna, Nigeria.

*** Corresponding Author:**
Azaki Gideon Philip
Address: Department of Chemistry, School of Physical Sciences, Federal University of Technology, Minna, Nigeria.
Phone: +234 (81) 60286039
E-mail: azakigideon@gmail.com, azaki.m1605498@st.futminna.edu.ng

Article info:
Received: 26 Jun 2025
Accepted: 21 Jul 2025

Keywords:
Iron oxides, Nanoparticles, Plant extracts, Antibacterial agents, Biological products

ABSTRACT

Background: The search for environmentally friendly nanomaterials with strong antimicrobial activity has generated growing interest in using plants to produce nanoparticles.

Objectives: This study aimed to biosynthesize and characterize iron (III) oxide (Fe_2O_3) nanoparticles stabilized by *Luffa cylindrica* extract and assess their antimicrobial properties.

Methods: The biosynthesized Fe_2O_3 nanoparticles were characterized using ultraviolet–visible (UV–Vis) spectroscopy, Fourier-transform infrared spectroscopy (FTIR), X-ray diffraction (XRD), scanning electron microscopy (SEM), and energy-dispersive X-ray spectroscopy to elucidate their optical, structural, morphological, and elemental properties.

Results: The formation of Fe_2O_3 nanoparticles was confirmed by standard absorbance at 370 nm and functional groups attributed to the capping and stabilization observed via FTIR. XRD patterns showed a crystalline rhombohedral phase, and SEM images indicated that the nanoparticles were uniformly dispersed with diameters of 20-50 nm. Nanoparticle efficacy was tested using the agar well diffusion method against a panel of gram-positive and gram-negative bacterial strains and fungal pathogens. The results revealed substantial dose-dependent antimicrobial activity, with greater inhibitory activity against *Staphylococcus aureus, Escherichia coli,* and *Candida albicans*, indicating potential broad-spectrum antimicrobial activity.

Conclusion: This study highlights the potential of *L. cylindrica*-mediated Fe_2O_3 nanoparticles as sustainable and effective antimicrobial agents with potential application in the biomedical, pharmaceutical, and environmental fields.

Citation Philip AG, Salihu AM, Ajoke FL, Yanda ShE, Timothy AU, Daniel T, et al. Characterization and Antimicrobial Activity of Biosynthesized Iron (III) Oxide Nanoparticles Stabilized by *Luffa cylindrica* Extract. Pharmaceutical and Biomedical Research. 2026; 12(1):49-60. http://dx.doi.org/10.32598/PBR.12.1.1422.1

http://dx.doi.org/10.32598/PBR.12.1.1422.1

Introduction

The emerging global rise in antimicrobial resistance has created a pressing need for new and sustainable antimicrobial agents. Nanotechnology has emerged as a novel, promising field over the past few years, providing sustainable solutions in the form of metal and metal oxide nanoparticles with potent antimicrobial properties. Iron (III) oxide (Fe_2O_3) nanoparticles have attracted significant attention due to their cost-effectiveness, magnetic properties, biocompatibility, and broad-spectrum antimicrobial efficacy [1, 2]. Conventional chemical synthesis of nanoparticles usually involves high energy consumption, hazardous byproducts, and toxic solvents [3]. To overcome these disadvantages, green synthesis methods involving biological entities, such as plant extracts, have gained considerable attention [4]. The green synthetic method is an eco-friendly route that leverages phytochemicals such as flavonoids, terpenoids, phenols, and alkaloids as natural reducing, stabilizing, and capping agents [5]. This method not only reduces environmental impact but also improves nanoparticle functionality through synergy with bioactive compounds [6]. *Luffa cylindrica*, commonly known as sponge gourd, is a medicinal plant widely distributed in tropical and subtropical regions [7], and its extracts are rich in bioactive compounds known for pharmacological activities such as antimicrobial, antioxidant, and anti-inflammatory activities [2, 7–9]. However, the use of this plant as a potential bio-template for nanoparticle synthesis remains poorly explored. Therefore, exploring its phytochemical profile for the fabrication of nanoparticles could stabilize them and improve their bioactivity. This study aimed to synthesize and characterize Fe_2O_3 nanoparticles using aqueous extracts of *L. cylindrica* and to evaluate their antimicrobial activity against selected clinically significant microbes. The exploration of green chemistry principles in nanomedicine contributes to the development of biocompatible and eco-conscious nanomaterials with favorable therapeutic and industrial applications.

Materials and Methods

Collection and preparation of plant material

Dried sponge gourd fruits of *L. cylindrica* were obtained from Gwada, Nigeria. The plant was identified and authenticated at the herbarium unit of the Department of Biological Sciences at Ahmadu Bello University, Zaria, Kaduna State, with voucher code ABU0298 deposited for reference. The gourds were washed to remove impurities and air-dried at room temperature for about 20 days. The pod was obtained from the dried sponge gourds and pulverised.

L. cylindrica pod extract preparation

Fresh *L. cylindrica* pods were thoroughly washed, chopped into small pieces, and air-dried for twenty days. The pods were obtained from the dried sponge gourds, then pulverised, and approximately 2 kg of the dried material was cold-macerated in 5 litres of distilled water at 70 ˚C for five days. The mixture was filtered using Whatman No. 1 filter paper, and a portion of the filtrate was stored at 4 ˚C until further use. The remaining filtrate was concentrated using a rotary evaporator and then dried in a water bath to obtain a crude extract.

Phytochemical screening of *L. cylindrica* extract

Qualitative phytochemical analysis

Phenols: To the filtrate (2 mL), 2–3 drops of freshly prepared 5% ferric chloride solution were added. The formation of a deep blue, bluish-black, or green coloration indicated a positive result for phenolic compounds [10].

Flavonoids: To 2 g of the extract, 1 mL of 2% sodium hydroxide (NaOH) solution was added. The mixture was gently shaken and allowed to stand for 2–3 minutes. The development of an intense yellow coloration, and a few drops of dilute hydrochloric acid (HCl) were added to the mixture, the disappearance or fading of the yellow color upon acidification indicated the presence of flavonoids [7].

Terpenoids: To 5 g of the extract, 2 mL of chloroform was added in a test tube and mixed thoroughly. Concentrated sulfuric acid (H_2SO_4) (3 mL) was carefully added along the side of the test tube to form a separate layer at the bottom. The formation of a reddish-brown coloration at the interface between two layers indicated the presence of terpenoids [11].

Saponins: To 3 g of the extract, 10 mL of distilled water was added to form a mixture. The mixture was filtered, and 5 mL of the aqueous extract was transferred to a test tube, vigorously shaken for 30 seconds, and then allowed to stand undisturbed for 15 minutes at room temperature. The formation and persistence of a stable froth layer lasting for more than 10 minutes indicated the presence of saponins [4].

Steroid: To 2 g of the chloroform extract, 2 mL of acetic anhydride was added, followed by the careful addition of 1–2 mL of concentrated H_2SO_4 along the side of the test tube to form a separate layer. The mixture was left undisturbed for 5–10 minutes. The formation of a bluish-green coloration at the interface indicated the presence of steroids [8].

Tannins: To the aqueous extract (2 mL), 10% lead acetate solution was added. The mixture was gently shaken and allowed to stand for 2–3 minutes. The formation of a yellowish precipitate indicated the presence of tannins [6].

Alkaloids: To the acidified extract (2 mL), a few drops of Mayer's reagent were added. The formation of a creamy white (turbidity) indicated the presence of alkaloids [5].

Quantitative phytochemical analysis

Phenol

A total of 0.1 g of the extract was dissolved in 10 mL of distilled water, to which 2.5 mL of 10% Folin-Ciocalteau reagent was added. The resulting mixture was neutralized with 2 mL of 7.5% sodium carbonate solution and incubated at 45 ˚C for 30 minutes. The absorbance of the mixture at 765 nm was measured using an ultraviolet (UV) spectrophotometer (UV-1800) [12].

Flavonoid

A total of 0.1 mL of 1 M sodium acetate was added to 0.5 mL of the extract, followed by 0.1 mL of pure methanol, 2.8 mL of distilled water, and 0.1 mL of 10% aluminum chloride. The resulting mixture was incubated for 30 minutes at room temperature, and the absorbance was measured at 415 nm using a UV-1800 [13].

Saponins

The extract (0.5 g) was dissolved in 20 mL of 1 N HCl and heated in a water bath for 4 hours. This solution was transferred to a conical flask to which 6 mL ferrous sulfate and 2 mL H_2SO_4 were added, followed by 5 mL of acetone-ethanol (1:1) mixture, and was allowed to stand for 10 minutes, and then allowed to evaporate, and later an absorbance of 490 nm was measured with a UV-1800 [8].

Tannins

A total of 0.2 g of the extract was dissolved in 20 mL of 50% methanol, wrapped with parafilm, and heated in a water bath at 80 ˚C for 1 hour. The mixture was then filtered, and to it were added 20 mL of deionized distilled water, 10 mL of sodium carbonate, and 2.5 mL of Folin reagent. This was followed by shaking the mixture well and leaving it to turn bluish-green in 20 minutes, and then an absorbance of 760 nm was measured with a UV spectrophotometer (UV-1800) [14].

Alkaloids

The extract (0.5 g) was diluted in 5 mL of a 1:1 mixture of 96% ethanol and 20% H_2SO_4, and then filtered through Whatman No. 1 filter paper. The filtrate was then diluted to 1 mL with 5 mL of 60% H_2SO_4 and left to stand for 5 minutes. It was then left at room temperature for 3 hours after 5 mL of 0.5% formaldehyde was poured after 5 minutes, and then the absorbance at 565 nm was measured by a UV-1800 [15].

Green synthesis of Fe_2O_3 nanoparticles

The green synthesis of Fe_2O_3 nanoparticles was achieved using *L. cylindrica* pod extract as a bio-reductant and stabilizing agent. First, twenty millilitres of 1 M ferric nitrate $Fe(NO_3)_3$ solution as precursor was introduced into 500 mL of freshly prepared plant extract under continuous stirring using a magnetic stirrer for 30 minutes at room temperature, after which 1 M NaOH solution was added gradually in dropwise to adjust the pH of the reaction mixture to neutral (pH 7.0). The reaction mixture was aged at room temperature (25–28 ˚C) overnight (12–16 hours) to permit complete reduction and nucleation of Fe^{3+} ions into iron oxide nanoparticles. The supernatant was carefully decanted, and the precipitated nanoparticle-rich lower layer was filtered using a Whatman No. 1 filter paper. The precipitate was thoroughly washed multiple times with distilled water until a clear, colorless filtrate was obtained, indicating the removal of unreacted precursors and soluble impurities. Subsequently, the washed residue was oven-dried at 80 ˚C for 3 hours to obtain dry F_2O_3 nanoparticles. The resulting Fe_2O_3 nanoparticles were stored in an airtight container for characterization [5, 6, 16] (Equation 1).

1. $$2Fe(NO_3)_{3\,(aq)} + \text{Plant Extract} + H_2O_{(l)} \xrightarrow[pH=7]{\text{Room temp}} Fe_2O_{3\,(s)} + \text{Biomolecules} + 6HNO_3$$

Characterization of iron oxide nanoparticles

Ultraviolet–visible (UV–Vis) spectrophotometry

The optical properties of the biosynthesized Fe_2O_3 nanoparticles were characterized using UV–Vis spectrophotometry to investigate the surface plasmon resonance (SPR) behavior, which is indicative of nanoparticle formation and stability. The analysis was performed using a double-beam UV–Vis spectrophotometer (Shimadzu UV-2600, Shimadzu Corporation, Kyoto, Japan) equipped with a 1.0 cm quartz cuvette. The instrument was operated at room temperature under ambient laboratory conditions. The nanoparticle suspension was diluted with deionized water to prevent signal saturation and ensure spectral accuracy. The UV–Vis absorption spectra were recorded over 200–700 nm at a scan rate of 400 nm/min and a spectral resolution of 1.0 nm. Baseline correction was performed using deionized water as a blank to eliminate background interference. The characteristic absorbance peak, typically associated with the SPR of Fe_2O_3 nanoparticles, was identified and monitored to confirm successful nanoparticle synthesis [17, 18].

Fourier-transform infrared spectroscopy (FTIR)

FTIR was employed to identify the bioactive functional groups present in the Fe_2O_3 nanoparticles reduced, stabilized, and capped by *L. cylindrica* pod extract. The analysis was conducted using a PerkinElmer Spectrum Two FTIR spectrometer (PerkinElmer Inc., Waltham, MA, USA) equipped with a deuterated triglycine sulfate detector and a KBr beam splitter. The dried plant extract and dried Fe_2O_3 nanoparticle powders were each finely ground and homogenized with spectroscopic-grade potassium bromide (KBr) at approximately 1:100 (sample: KBr w/w), then pressed into transparent pellets using a hydraulic press at ~10 tons for 2 minutes. Each pellet was scanned over a spectral range of 4000–400 cm^{-1} with a resolution of 4 cm^{-1}, and 32 consecutive scans per sample were averaged to enhance signal-to-noise ratio [19, 20].

X-ray diffraction (XRD)

The crystalline structure and phase purity of the biosynthesized Fe_2O_3 nanoparticles were determined using the XRD method derived from [21] and [1]. The analysis was performed with a PANalytical X Pert PRO diffractometer (Malvern PANalytical, Almelo, The Netherlands), which was operated at 40 kV and 30 mA with Cu-Kalpha monochromatized radiation of 1.5406 Å wavelength. The dried nanoparticle powder was uniformly sprinkled onto a sample holder and scanned over 10–80° with a scanning speed of 0.02°/s and a step size of 0.02°. Data were collected and interpreted using the X'Pert HighScore Plus software, and the patterns obtained were compared with international standard reference data in the joint committee on powder diffraction standards (JCPDS) database to confirm the crystalline phase and the formation of Fe_2O_3. The nanoparticles' size was measured in an average of crystallite dimension (D) using the Debye Scherrer (Equation 2):

$$2.\ D = \frac{K\lambda}{\beta COS\theta}$$

Where:

D is the average crystallite size (in nm), K is the Scherrer constant (typically 0.9), λ is the X-ray wavelength (1.5406 Å), β is the full width at half maximum of the most intense diffraction peak (in radians), and θ is the Bragg angle (in degrees).

Scanning electron microscopy (SEM) analysis

SEM was used to determine the surface morphology and microstructural characteristics of the biosynthesized Fe_2O_3 nanoparticles. Imaging was performed with a Zeiss EVO 18 scanning electron microscope (Carl Zeiss Microscopy GmbH, Jena, Germany), operated under high-vacuum conditions. A total of 0.05 g of the dried nanoparticle powder was gently sprinkled onto carbon adhesive tape affixed to a standard aluminum stub. The sample was coated with a thin conductive layer of gold-palladium alloy (Au: Pd; 60:40) using a Quorum T150Y sputter coater (Quorum Technologies Ltd., UK) for 5 minutes at a current of 20 mA under an argon atmosphere to improve conductivity and minimize charging during imaging [13].

Energy-dispersive X-ray (EDX) analysis

The elemental compositions of the synthesized nanoparticles were determined using EDX spectroscopy. EDX spectra were collected over the energy range 0–20 keV, with a live acquisition time of 60 seconds to obtain an accurate signal. Elemental analysis was quantitatively assessed using vendor-developed modern software with conventional ZAF (atomic number, absorption, and fluorescence) matrix corrections. The peaks in the X-ray spectra (Fe (Kalpha ~6.4keV) and oxygen (Kalpha 0.53 keV) confirmed the iron oxide nature of the nanoparticles. The percentages of element-weights were calculated from the data provided as Mean±SD from three independent spectral acquisitions representing the different areas of the sample to evaluate constituent dispersion over the sample surface [13, 22].

Antimicrobial activity assay

The antimicrobial efficacy of the biosynthesized Fe_2O_3 nanoparticles was evaluated in vitro against selected pathogenic microorganisms, including two bacterial strains, *Staphylococcus aureus* (ATCC 25923), and *Escherichia coli* (ATCC 25922), and a fungal strain, *Candida albicans* (ATCC 10231). The assay was conducted using the agar well diffusion method, a widely adopted technique for preliminary screening of antimicrobial agents [23].

Preparation of test microbial inocula

Fresh colonies of each microbial strain were inoculated into nutrient broth (for bacteria) and Sabouraud dextrose broth (for *C. albicans*) and incubated at 37 ˚C for 18–24 h (bacteria) or 28 ˚C for 48 h (fungus). The turbidity of each culture was adjusted to match a 0.5 McFarland standard (approximately 1×10^8 CFU/mL for bacteria and 1×10^6 CFU/mL for *C. albicans*).

Agar well diffusion method

Sterile mueller–hinton agar plates (for bacterial strains) and sabouraud dextrose agar plates (for fungal strains) were prepared and allowed to solidify. Each standardized microbial suspension was evenly spread over the agar surface using a sterile cotton swab to ensure uniform growth. Wells of 6 mm diameter were punched aseptically into the agar using a sterile cork borer. The Fe_2O_3 nanoparticle suspension at concentrations of 200, 400, 600, 800, and 1000 mg/mL was prepared in sterile distilled water. Aliquots (100 µL) of each concentration were introduced into the respective wells. The plates were incubated at 37 ˚C for 24 hours (bacteria) and 28 ˚C for 48 hours (fungus) under aerobic conditions. Standard antibiotics, ciprofloxacin (10 mg/mL) for bacteria [24] and amphotericin B (25 mg/mL) for *C. albicans*, were used as controls, and after incubation, zones of inhibition around the wells were measured in millimeters (mm) using a digital caliper.

Statistical analysis

The values obtained from all experiments were conducted in triplicate and presented as Mean±SD. To evaluate significant differences among treatments, one-way analysis of variance followed by Tukey's post hoc test was performed using SPSS software, version 26. The significance level was set at $P<0.05$.

Results

Percentage yield of *L. cylindrica* pod extract

The *L. cylindrica* pod extract was subjected to preliminary physical evaluation to assess its yield, consistency, and visual appearance. The result revealed a brownish, solid mass, weighing 552 g, which corresponded to a percentage yield of 27.6% in Table 1.

Discussion

Percentage yield and phytochemical screening

L. cylindrica pods extract yielded a solid brown mass with a distinct yellow color, weighing 552 g, corresponding to a 27.6% yield (Table 1). This yield suggests a relatively efficient recovery of phytochemicals under the employed extraction conditions, consistent with previous reports on cucurbitaceous plants known for their resinous and phenolic content. This study was compared with [11], which reported yields of 25–30% from *Lagenaria siceraria*, confirming that the genus is rich in extractable secondary metabolites. Table 2 presents the qualitative phytochemical screening for the presence of key bioactive groups, such as phenols, flavonoids, saponins, tannins, and alkaloids. Although terpenoids and steroids were absent, this composition provides an insight into the therapeutic potential of the extract, particularly due to the synergy often reported among phenolic and flavonoid compounds in antioxidant and antimicrobial actions [8]. The turbidity and frothing observed in the saponin test confirmed the presence of these compounds and are consistent with earlier observations in *Luffa* species [24]. Terpenoids and steroids were absent, which may be attributed to the part of the plant used or to the polarity of the extraction solvent because previous studies have documented their presence predominantly

Table 1. Yield of *L.cylidrical* pod extract in percentage

Colour	Appearance	Weight (g)	Yield (%)
Yellow	Solid brown mass	552	27.6

Table 2. Qualitative phytochemical screening

Phytochemical	Observation	Inference
Phenols	Red-brown colour	+
Flavonoids	Yellow colour	+
Terpenoids	Reddish-brown colour	-
Saponins	Froth emulsion	+
Steroids	Blue to dark-blue colour	-
Tannins	Yellowish precipitate	+
Alkaloids	Turbidity present	+

(-): Absence; (+): Present.

PBR

in the leaves and roots of *L. cylindrica* under methanolic or hexane extraction protocols [25]. The quantitative phytochemical screening in Table 3 showed that phenols (34.78 mg/100 g) were the most abundant phytochemical, constituting 30.16% of the total phytochemical composition, followed by saponins (30.1 mg/100 g; 26.1%), flavonoids (24.2 mg/100 g; 20.99%), tannins (18 mg/100 g; 15.61%), and alkaloids (8.23 mg/100 g; 7.14%). The values were significantly different ($P<0.05$), indicating that phenolics dominate the biochemical profile of the pod extract. The high phenolic and flavonoid content in *L. cylindrica* pod extract indicates strong antioxidant potential, as both classes are well documented for their radical-scavenging abilities and protective roles in oxidative stress-related pathologies [26]. Saponins were over a quarter of the total phytochemical load; their membrane-permeabilizing effect contributes significantly to antimicrobial activity [27]. Although the amounts of both tannins and alkaloids were low, their antimicrobial, cytotoxic properties, microbial growth inhibition, and apoptosis induction in cancer cells have been studied [28].

Characterization of biosynthesized Fe_2O_3 nanoparticles

The optical differences between the bulk and biosynthesized Fe_2O_3, as observed in the figure, were evident in UV-Vis absorption spectra and indicated variations in particle size, surface chemistry, and electronic structure. In bulk Fe_2O_3, a relatively broad and less intense absorption profile was observed with a maximum absorbance centered around 490–500 nm, which is consistent with ligand-to-metal charge transfer transitions from O^{2-} to Fe^{3+} within the hematite lattice. This broader band with less pronounced features characterizes larger, micron-sized particles with a low surface area-to-volume ratio and limited quantum confinement [29]. In contrast, the UV-Vis spectrum of the biosynthesized Fe_2O_3 nanoparticles (Figure 1), showed a distinct and sharper absorption peak in the range of 390–400 nm, with a blue shift in the absorption edge compared to the bulk counterpart. This shift can be linked to the quantum confinement effect associated with reduced particle size at the nanoscale [30]. Enhancements in peak sharpness and intensity

Table 3. Quantitative phytochemical screening

Phytochemicals	Mean±SD Results (mg/100)	(%)
Phenols	34.78±0.01^{e}	30.16
Flavonoids	24.20±0.04^{c}	20.99
Saponins	30.10±0.02^{d}	26.10
Tannins	18.00±0.01^{b}	15.61
Alkaloids	8.23±0.00^{a}	7.14

PBR

Note: Values with different superscript letters (a–e) within the same column are significantly different at $P<0.05$.

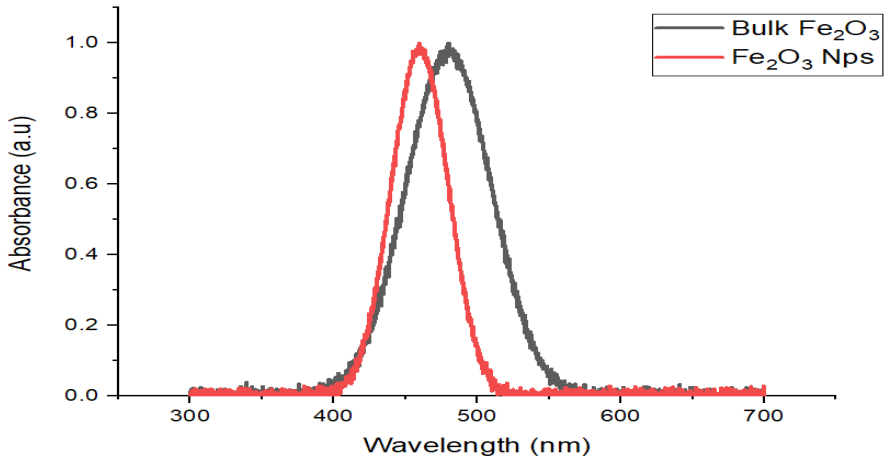

PBR

Figure 1. U-Vis spectrum for bulk Fe_2O_3 and biosynthesized Fe_2O_3 nanoparticles

were observed, further reflecting improved electronic transitions due to higher surface reactivity and reduced agglomeration, probably stabilized by the phytochemicals present in *L. cylindrica* pod extract [31]. These bioactive compounds could have contributed to modifying surface states, enhancing additional electronic interactions, and tuning the optical bandgap [32]. Therefore, the spectral sharpening and blue shift observed in the Fe_2O_3 nanoparticle confirmed the successful synthesis at the nanoscale with a changed band structure that provided these nanoparticles with potent antimicrobial properties.

Figure 2 shows the FTIR spectrum of the biosynthesized Fe_2O_3 nanoparticles, which exhibited characteristic absorption bands indicating both the presence of iron oxide and functional groups, derived from *L. cylindrica* pod extract. A broad absorption band observed approximately 3400 cm^{-1} corresponds to O–H stretching vibrations, probably arising from hydroxyl present in polyphenols, or saponins present in the plant extract [33]. Peaks around 2900–2800 cm^{-1} were observed and assigned to aliphatic C–H stretching vibrations, indicating the presence of long-chain organic molecules capping the nanoparticle surface [34]. A prominent band

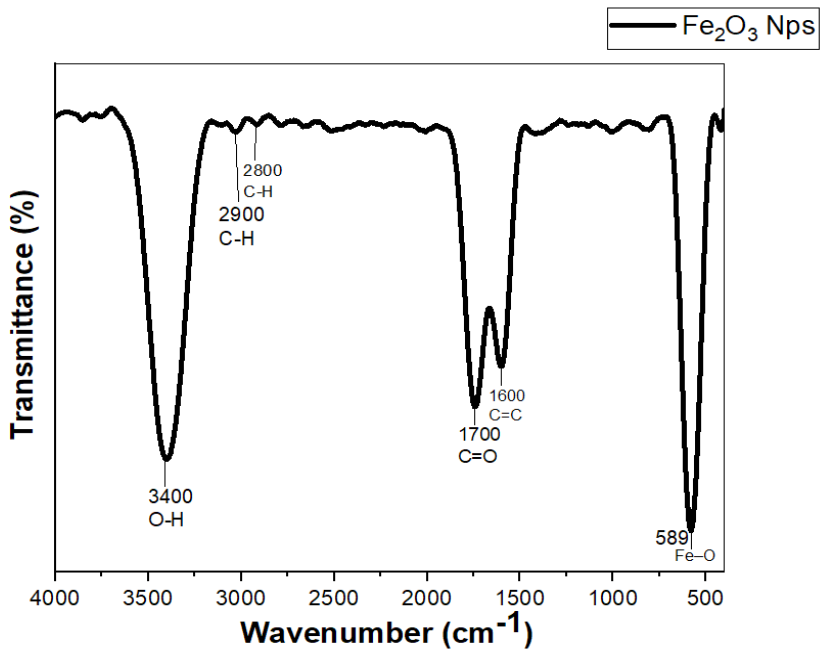

PBR

Figure 2. FTIR spectrum of biosynthesized Fe_2O_3 nanoparticles

Table 4. Zone of inhibition of biosynthesized Fe_2O_3 nanoparticles compared with controls

Test Microorganisms	Mean±SD						
	Concentration					Standard Antibiotics	
	200 mg/mL	400 mg/mL	600 mg/mL	800 mg/mL	1000 mg/mL	Ciprofloxacin	Amphotericin B
Staphylococcus	11.1±0.01[a]	12.1±0.1[a]	16.2±0[a]	20±0.01[a]	31.6±0.1[b]	16.2±0.2[b]	2.3±0.02[a]
E. coli	12.3±0.02[b]	14.5±0.03[b]	17.4±0.01[b]	22.1±0.02[b]	50.2±0.3[c]	20±0.02[c]	3±0.1[b]
C. albicans	13.2±0.01[c]	15.3±0.02[c]	19.1±0.04[c]	24±0[c]	25.2±0.01[a]	5.8±0[a]	20.2±0[c]

PBR

Note: Values with different superscript letters (a–e) within the same column are significantly different at P<0.05.

at ~1700 cm^{-1} corresponds to C=O stretching, suggesting the presence of carbonyl functional groups, such as flavonoids, in the plant extract [35]. The region around 1600 cm^{-1} showed a moderate band ascribed to C=C stretching of aromatic systems [21], which further supports the involvement of phytochemicals in nanoparticle stabilization. Essentially, a strong Fe–O stretching vibration at 589 nm, as also reported by [36], is characteristic of the metal–oxygen bond in α-Fe_2O_3. These findings confirm the successful formation of Fe_2O_3 nanoparticles and demonstrate the role of phytochemicals from the *L. cylindrica* extract as both reducing and capping agents during the green synthesis process.

In Figure 3, the XRD patterns showed distinct diffraction peaks at 2θ values of approximately 25.1°, 33.2°, 35.6°, 49.8°, 54.7°, 62.4°, and 64.9°, which correspond to the (012), (104), (110), (113), (024), (116), and (214) crystallographic planes respectively. These reflections are characteristic of a hematite (α-Fe_2O_3) rhombohedral crystal structure and agree with JCPDS Card No. 33-0664. Both sharp and intense peaks were present, confirming the crystalline nature of the synthesized nanoparticles; however, the broadening of the peaks observed suggested nanoscale dimensions and possible lattice strain induced by capping agents from the *L. cylindrica* pod extract [37]. The XRD pattern did not reveal additional peaks indicating phase purity, with no detectable impurities or secondary iron phases, such as maghemite (γ-Fe_2O_3) or magnetite (Fe_2O_3). The calculated crystallite size of 34.5 nm using the Debye–Scherrer equation confirmed the nanocrystalline nature of the sample and highlights the effectiveness of the green synthesis route in producing stable, phase-pure α-Fe_2O_3 nanoparticles.

Figure 4 shows the surface morphology and elemental composition of the green-synthesized Fe_2O_3 nanoparticles determined using SEM attached with EDX. The micrographs obtained from SEM show that the nanoparticles revealed quasi-spherical to slightly irregular mor-

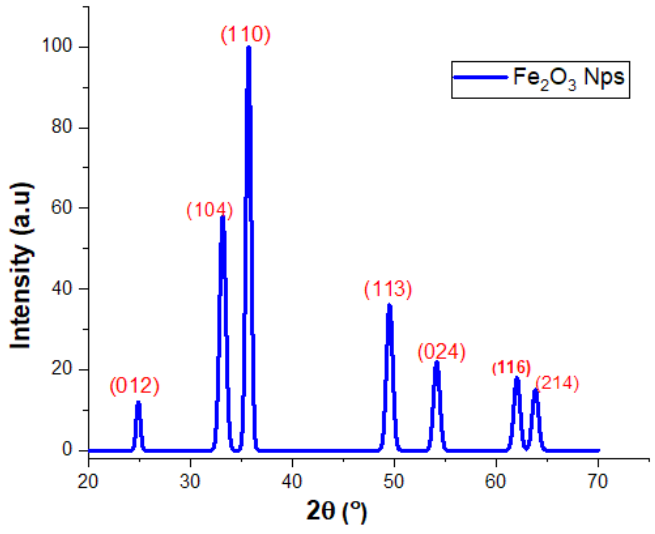

Figure 3. XRD pattern of biosynthesized Fe_2O_3 nanoparticles

PBR

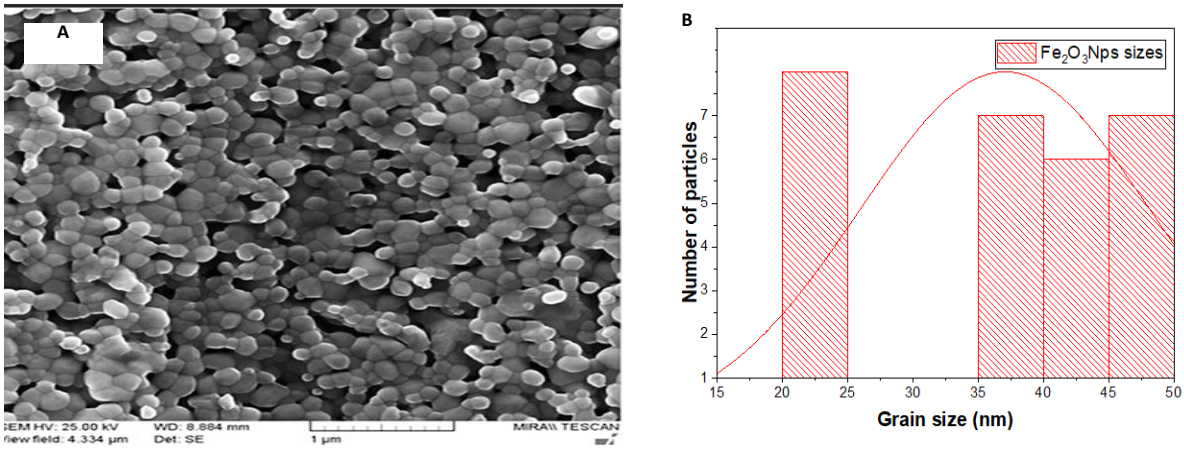

Figure 4. A) SEM micrographs of biosynthesized Fe_2O_3 nanoparticles, B) A graph of Fe_2O_3 nanoparticles size distribution

phologies, as well as agglomeration. This character in biosynthesized nanomaterials is attributed to hydrogen bonding and van der Waals interactions among surface-bound phytochemicals [38]. The grain sizes of the Fe_2O_3 nanoparticles were predominantly within the range of 20–50 nm, with an average of 35 nm, which is consistent with nanoscale dimensions. This size is consistent with the dimensions reported by [39]. The capping agents present in *L. cylindrica* pod extract likely contributed to the relatively uniform size and smooth surface textures observed. Clustered nanoparticle arrangements were observed in some areas, possibly due to organic residues acting as a mild binder or secondary aggregation during drying. Figure 5 confirmed the elemental composition; the matching EDX pattern corresponds to the nanomaterial synthesized, showing strong peaks for iron (Fe) and oxygen (O), validating the formation of iron oxide. Remarkably, the Fe-to-O atomic ratio was equal to the stoichiometry of Fe_2O_3, supporting the phase identity indicated by XRD analysis. Weak signals for other elements, such as carbon, potassium, and nitrogen, although insignificant, were detected and could be attributed to residual phytochemicals from *L. cylindrica*.

Antimicrobial activity of biosynthesized Fe_2O_3 nanoparticles

The biosynthesized Fe_2O_3 nanoparticles exhibited measurable inhibition zones against *S. aureus*, *E. coli*, and *C. albicans* (Table 4). This activity aligns with recent reports on green-synthesized iron oxide nanoparticles showing notable antimicrobial effects [1, 6]. Mechanistically, the antimicrobial effect is likely due to the induction of oxidative stress via reactive oxygen species (ROS), disruption of cell membrane integrity, and DNA damage. Such effects have been documented in green-synthesized hematite (α-Fe_2O_3) nanoparticles [6]. Notably, gram-positive *S. aureus* was more susceptible

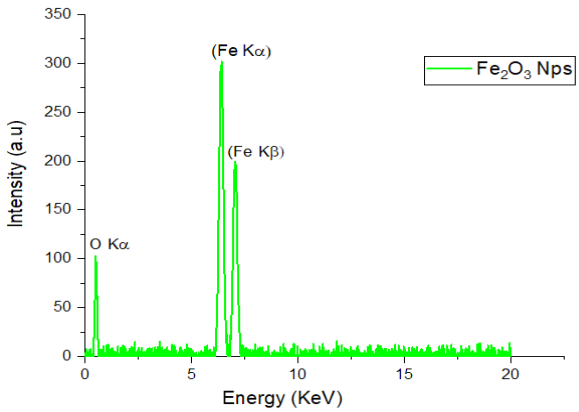

Figure 5. EDX spectrum of biosynthesized Fe_2O_3 nanoparticles

than gram-negative *E. coli*, consistent with prior observations that gram-positive bacteria are generally more vulnerable to Fe_2O_3 nanoparticle action due to their differing cell wall architecture [1]. In a further study, [39] demonstrated that α-Fe_2O_3 nanoparticles synthesized via microbial routes exhibited potent antibacterial, antibiofilm, and anti-virulence properties against pathogenic bacteria. A similar study by [40], who evaluated iron oxide nanoparticles synthesized with *Melia azedarach* leaf extract, observed strong antimicrobial activity against diarrheagenic pathogens, with low cytotoxicity [41-43]. reported that alginate-stabilized Fe_2O_3 nanoparticles exhibited strong inhibitory activity against various clinical isolates, including *S. aureus*, *Bacillus subtilis*, and *C. albicans*, confirming antimicrobial potency, which was consistent with this study. These studies consistently attribute part of the enhanced activity to phytochemical capping agents that confer stability [44, 45] and bioactive synergy to the nanoparticles [46-48]. A clear concentration-dependent increase in antimicrobial efficacy was observed, indicating that higher nanoparticle concentrations yield proportionately larger inhibition zones. This dose–response trend reflects increased nanoparticle availability and uptake, similar to previous works observed by other researchers [49-51].

Conclusion

This study reported the green synthesis and stabilization of Fe_2O_3 nanoparticles using *L. cylindrica* pod extract as an eco-friendly and sustainable alternative to traditional chemical methods. The characterized nanoparticles revealed desirable properties, such as functional group interactions attributed to bioactive compounds in the extract, crystallinity, and nanoscale morphology. Moreover, biosynthesized Fe_2O_3 nanoparticles showed broad-spectrum antimicrobial activity against both gram-negative and gram-positive bacterial strains, with a dose-dependent inhibitory effect. However, further studies, including determination of minimum inhibitory concentrations, minimum bactericidal concentrations, and time-kill kinetics, are recommended.

Ethical Considerations

Compliance with ethical guidelines

There were no ethical considerations to be considered in this research.

Funding

This research did not receive any grant from funding agencies in the public, commercial, or non-profit sectors.

Authors' contributions

Conceptualization, methodology, project administration and supervision: Fadipe Labake Ajoke; Data collection: Suleiman Rahmat, Agbai Uche Timothy, James Daniel Shaba and Elijah Yanda; Formal analysis and investigation: Agbai Uche Timothy, James Daniel Shaba and Elijah Yanda; Writing: Suleiman Rahmat and Azaki Gideon Philip; Visualization: Azaki Gideon Philip and Salihu Aliyu Makanta.

Conflict of interest

The authors declared no conflict of interest.

Acknowledgments

The authors gratefully acknowledge the support of all affiliated institutions for providing laboratory facilities and technical assistance throughout this research.

References

[1] Takahashi K, Sekizuka T, Fukumoto H, Nakamichi K, Suzuki T, Sato Y, et al. Deep-sequence identification and role in virus replication of a JC virus quasispecies in patients with progressive multifocal leukoencephalopathy. J Virol. 2016; 91(1):e01335-16. [DOI:10.1128/JVI.01335-16] [PMID]

[2] Kartau M, Verkkoniemi-Ahola A, Paetau A, Palomäki M, Janes R, Ristola M, et al. The incidence and predisposing factors of John Cunningham virus-induced progressive multifocal leukoencephalopathy in Southern Finland: A population-based study. Open Forum Infect Dis. 2019; 6(2):ofz024. [DOI:10.1093/ofid/ofz024] [PMID]

[3] Suleman M, Khan TA, Ejaz H, Maroof S, Alshammari A, Albekairi NA, et al. Structural vaccinology, molecular simulation and immune simulation approaches to design multi-epitopes vaccine against John Cunningham virus. Microb Pathog. 2024; 189:106572. [DOI:10.1016/j.micpath.2024.106572] [PMID]

[4] Vilibic-Cavlek T, Bogdanic M, Peric T, Radmanic L, Antolasic L, Milasincic L, et al. Prevalence of JC polyomavirus in patients with neuroinvasive disease of unknown etiology in Croatia. Medicina. 2024; 60(1):69. [DOI:10.3390/medicina60010069] [PMID]

[5] Zou W, Imperiale MJ. Biology of polyomavirus miRNA. Front Microbiol. 2021; 12:662892. [DOI:10.3389/fmicb.2021.662892] [PMID]

[6] Delbue S, Comar M, Ferrante P. Review on the role of the human Polyomavirus JC in the development of tumors. Infect Agent Cancer. 2017; 12:10. [DOI:10.1186/s13027-017-0122-0] [PMID]

[7] Maginnis MS, Atwood WJ. JC virus: An oncogenic virus in animals and humans? Semin Cancer Biol. 2009; 19(4):261-9. [DOI:10.1016/j.semcancer.2009.02.013] [PMID]

[8] Dwyer C, Sharmin S, Kalincik T. Rates of John cunningham virus seroconversion greatly reduced in natalizumab-treated patients during COVID-19-related lockdowns. Eur J Neurol. 2024; 31(1):e16059. [DOI:10.1111/ene.16059] [PMID]

[9] Del Valle L, Khalili K. Induction of brain tumors by the archetype strain of human neurotropic JCPyV in a transgenic mouse model. Viruses. 2021; 13(2):162. [DOI:10.3390/v13020162] [PMID]

[10] Sgarlata E, Chisari CG, Toscano S, Finocchiaro C, Lo Fermo S, Millefiorini E, et al. Changes in John cunningham virus index in multiple sclerosis patients treated with different disease-modifying therapies. Curr Neuropharmacol. 2022; 20(10):1978-87. [DOI:10.2174/1570159X19666211111123202] [PMID]

[11] Flores J, Anguiano O, Rivas-Alonso V, González-Conchillos H, Pérez-Saldivar M, Sotelo J, et al. Mutations in the John Cunningham virus VP1 gene could predispose to the development of progressive multifocal leukoencephalopathy in multiple sclerosis patients undergoing treatment with natalizumab. Mult Scler Relat Disord. 2021; 56:103266. [DOI:10.1016/j.msard.2021.103266] [PMID]

[12] Bhaskar Kalarani I, Thasneem K, Veerabathiran R. Chapter 5 - Oncoviruses: Future prospects of molecular mechanisms and therapeutic strategies. In: Ennaji MM, editor. Oncogenic Viruses. Cambridge: Academic Press; 2023. [DOI:10.1016/B978-0-12-824156-1.00012-1]

[13] Muhsen M Ali Z, Ghaith Sachit H, Jaafar Hussein M, Mohammed Ali SH, Mohammed Al-Alwany SH, Khalil Hussein A. Molecular interplay of John Cunningham virus with interleukin 1 beta in colorectal carcinomatous tissues from a group of Iraqi patients. Arch Razi Inst. 2022; 77(6):2299-306. [DOI:10.22092/ARI.2022.358617.2267] [PMID]

[14] Zheng HC, Xue H, Zhang CY. The oncogenic roles of JC polyomavirus in cancer. Front Oncol. 2022; 12:976577. [DOI:10.3389/fonc.2022.976577] [PMID]

[15] Ikegaya H. Geographical identification of cadavers by human parasites. Forensic Sci Int Genet. 2008; 2(2):83-90. [DOI:10.1016/j.fsigen.2007.10.184] [PMID]

[16] Butic AB, Spencer SA, Shaheen SK, Lukacher AE. Polyomavirus wakes up and chooses neurovirulence. Viruses. 2023; 15(10):2112. [DOI:10.3390/v15102112] [PMID]

[17] Mettenleiter TC. Breaching the barrier-the nuclear envelope in virus infection. J Mol Biol. 2016; 428(10 Pt A):1949-61. [DOI:10.1016/j.jmb.2015.10.001] [PMID]

[18] Cortese I, Reich DS, Nath A. Progressive multifocal leukoencephalopathy and the spectrum of JC virus-related disease. Nat Rev Neurol. 2021; 17(1):37-51. [DOI:10.1038/s41582-020-00427-y] [PMID]

[19] Ferenczy MW, Marshall LJ, Nelson CD, Atwood WJ, Nath A, Khalili K, et al. Molecular biology, epidemiology, and pathogenesis of progressive multifocal leukoencephalopathy, the JC virus-induced demyelinating disease of the human brain. Clin Microbiol Rev. 2012; 25(3):471-506. [DOI:10.1128/CMR.05031-11] [PMID]

[20] Torres C. Evolution and molecular epidemiology of polyomaviruses. Infect Genet Evol. 2020; 79:104150. [DOI:10.1016/j.meegid.2019.104150] [PMID]

[21] Mouliou DS. John cunningham virus and progressive multifocal leukoencephalopathy: A falsely played diagnosis. Diseases. 2024; 12(5):100. [DOI:10.3390/diseases12050100] [PMID]

[22] Bhattacharjee S, Chattaraj S. Entry, infection, replication, and egress of human polyomaviruses: an update. Can J Microbiol. 2017; 63(3):193-211. [DOI:10.1139/cjm-2016-0519] [PMID]

[23] Imperiale MJ. The human polyomaviruses: An overview. In: Khalili K, Stoner GL, editors. Human polyomaviruses: Molecular and clinical perspectives. Hoboken: Wiley; 2001. [Link]

[24] Ahye N, Bellizzi A, May D, Wollebo HS. The role of the JC virus in central nervous system tumorigenesis. Int J Mol Sci. 2020; 21(17):6236. [DOI:10.3390/ijms21176236] [PMID]

[25] Fadipe LA, Ajemba C, Lawal BA, Ahmadu AA, Ibikunle GF, et al. Phytochemical and In-vivo Antimalarial Investigations of Dichrostachys cinerea (L.) Wight & Arn. (Fabaceae) Root Bark. Trop J Nat Prod Res. 2020; 4(11):1007–14. [Link]

[26] Xu Y, Tao R, Li J, Ou T. JC polyomavirus infection and its noncoding control region mutations in bladder cancer. Hoboken: Wiley; 2025. [DOI:10.22541/au.175093397.79712262/v1]

[27] Ajuh ET, Wu Z, Kraus E, Weissbach FH, Bethge T, Gosert R, et al. Novel human polyomavirus noncoding control regions differ in bidirectional gene expression according to host cell, large T-antigen expression, and clinically occurring rearrangements. J Virol. 2018; 92(7):e02231-17. [DOI:10.1128/JVI.02231-17] [PMID]

[28] Khalili K, White MK, Sawa H, Nagashima K, Safak M. The agnoprotein of polyomaviruses: A multifunctional auxiliary protein. J Cell Physiol. 2005; 204(1):1-7. [DOI:10.1002/jcp.20266] [PMID]

[29] Saribas AS, Coric P, Hamazaspyan A, Davis W, Axman R, White MK, et al. Emerging from the unknown: Structural and functional features of agnoprotein of polyomaviruses. J Cell Physiol. 2016; 231(10):2115-27. [DOI:10.1002/jcp.25329] [PMID]

[30] Ricciardiello L, Baglioni M, Giovannini C, Pariali M, Cenacchi G, Ripalti A, et al. Induction of chromosomal instability in colonic cells by the human polyomavirus JC virus. Cancer Res. 2003; 63(21):7256-62. [Link]

[31] Mushtaq M, Darekar S, Kashuba E. DNA tumor viruses and cell metabolism. Oxid Med Cell Longev. 2016; 2016:6468342. [DOI:10.1155/2016/6468342] [PMID]

[32] He J, Liu L, Tang F, Zhou Y, Liu H, Lu C, et al. Paradoxical effects of DNA tumor virus oncogenes on epithelium-derived tumor cell fate during tumor progression and chemotherapy response. Signal Transduct Target Ther. 2021; 6(1):408. [DOI:10.1038/s41392-021-00787-x] [PMID]

[33] Moens U, Van Ghelue M, Ehlers B. Are human polyomaviruses co-factors for cancers induced by other oncoviruses? Rev Med Virol. 2014; 24(5):343-60. [DOI:10.1002/rmv.1798] [PMID]

[34] White MK, Khalili K. Expression of JC virus regulatory proteins in human cancer: Potential mechanisms for tumourigenesis. Eur J Cancer. 2005; 41(16):2537-48. [DOI:10.1016/j.ejca.2005.08.019] [PMID]

[35] Sinagra E, Raimondo D, Gallo E, Stella M, Cottone M, Rossi F, et al. JC virus and lung adenocarcinoma: Fact or myth? Anticancer Res. 2017; 37(6):3311. [DOI:10.21873/anticanres.11699]

[36] Reiss K, Khalili K. Viruses and cancer: Lessons from the human polyomavirus, JCV. Oncogene. 2003; 22(42):6517-23. [DOI:10.1038/sj.onc.1206959] [PMID]

[37] Ksiaa F, Ziadi S, Mokni M, Korbi S, Trimeche M. The presence of JC virus in gastric carcinomas correlates with patient's age, intestinal histological type and aberrant methylation of tumor suppressor genes. Mod Pathol. 2010; 23(4):522-30. [DOI:10.1038/modpathol.2009.184] [PMID]

[38] Noch E, Sariyer IK, Gordon J, Khalili K. JC virus T-antigen regulates glucose metabolic pathways in brain tumor cells. Plos One. 2012; 7(4):e35054. [DOI:10.1371/journal.pone.0035054] [PMID]

[39] Muñoz-Mármol AM, Mola G, Ruiz-Larroya T, Fernández-Vasalo A, Vela E, Mate JL, et al. Rarity of JC virus DNA sequences and early proteins in human gliomas and medulloblastomas: The controversial role of JC virus in human neurooncogenesis. Neuropathol Appl Neurobiol. 2006; 32(2):131-40. [DOI:10.1111/j.1365-2990.2006.00711.x] [PMID]

[40] White MK, Gordon J, Reiss K, Del Valle L, Croul S, Giordano A, et al. Human polyomaviruses and brain tumors. Brain Res Brain Res Rev. 2005; 50(1):69-85. [DOI:10.1016/j.brainresrev.2005.04.007] [PMID]

[41] Soltani S, Farahani A, Shahbahrami R, Shateri Z, Emadi MS, Pakzad R, et al. Investigation of epstein-barr virus, cytomegalovirus, human herpesvirus 6, and polyoma viruses (JC virus, BK virus) among Gastric cancer patients: A cross sectional study. Health Sci Rep. 2024; 7(4):e2043. [DOI:10.1002/hsr2.2043] [PMID]

[42] Izi S, Youssefi M, Rahmani F, Roshan NM, Yari A, Avval FZ. Detection of JC Polyomavirus tumor antigen in gastric carcinoma: A report from Iran. Iran J Microbiol. 2018; 10(4):266-74. [PMID]

[43] Yamaoka S, Yamamoto H, Nosho K, Taniguchi H, Adachi Y, Sasaki S, et al. Genetic and epigenetic characteristics of gastric cancers with JC virus T-antigen. World J Gastroenterol. 2009; 15(44):5579-85. [DOI:10.3748/wjg.15.5579] [PMID]

[44] Haghi Navand A, Teimoori A, Makvandi M, Nisi N, Seyedian SS, Ranjbari N, et al. Study on JV virus in patients with colon cancer type adenocarcinoma. Asian Pac J Cancer Prev. 2019; 20(4):1147-51. [DOI:10.31557/APJCP.2019.20.4.1147] [PMID]

[45] Prezioso C, Pietropaolo V, Moens U, Ciotti M. JC polyomavirus: A short review of its biology, its association with progressive multifocal leukoencephalopathy, and the diagnostic value of different methods to manifest its activity or presence. Expert Rev Mol Diagn. 2023; 23(2):143-57. [DOI:10.1080/14737159.2023.2179394] [PMID]

[46] Shin SK, Li MS, Fuerst F, Hotchkiss E, Meyer R, Kim IT, et al. Oncogenic T-antigen of JC virus is present frequently in human gastric cancers. Cancer. 2006; 107(3):481-8. [DOI:10.1002/cncr.22028] [PMID]

[47] Abdel-Aziz HO, Murai Y, Hong M, Kutsuna T, Takahashi H, Nomoto K, et al. Detection of the JC virus genome in lung cancers: possible role of the T-antigen in lung oncogenesis. Appl Immunohistochem Mol Morphol. 2007; 15(4):394-400. [DOI:10.1097/01.pai.0000213126.96590.64] [PMID]

[48] Alibek K, Kakpenova A, Mussabekova A, Sypabekova M, Karatayeva N. Role of viruses in the development of breast cancer. Infect Agent Cancer. 2013; 8:32. [DOI:10.1186/1750-9378-8-32] [PMID]

[49] Hachana M, Amara K, Ziadi S, Gacem RB, Korbi S, Trimeche M. Investigation of human JC and BK polyomaviruses in breast carcinomas. Breast Cancer Res Treat. 2012; 133(3):969-77. [DOI:10.1007/s10549-011-1876-5] [PMID]

[50] James LM, Georgopoulos AP. Breast cancer, viruses, and human leukocyte antigen (HLA). Sci Rep. 2024; 14(1):16179. [DOI:10.1038/s41598-024-65707-9] [PMID]

[51] Del Valle L, White MK, Enam S, Piña Oviedo S, Bromer MQ, Thomas RM, et al. Detection of JC virus DNA sequences and expression of viral T antigen and agnoprotein in esophageal carcinoma. Cancer. 2005; 103(3):516-27. [DOI:10.1002/cncr.20806] [PMID]